Dual-frequency car-borne DInSAR at L-band and Ku-band for mobile mapping of surface displacements

Othmar Frey
Gamma Remote Sensing, Gümligen, Switzerland / ETH Zurich, Switzerland
Email: frey@gamma-rs.ch / otfrey@ethz.ch

Charles L. Werner, Rafael Caduff
Gamma Remote Sensing, Gümligen, Switzerland
Email: cw@gamma-rs.ch / caduff@gamma-rs.ch

Abstract

We present our recent developments and experimental results on car-borne mobile mapping of ground-surface displacements with our in-house-developed SAR systems. Recently, we have successfully demonstrated car-borne and UAV-borne DInSAR with the Gamma L-band SAR system. Meanwhile we have upgraded our car-borne measurement configuration that now permits acquiring simultaneously at L-band and at Ku-band. We show first interferometric results with short temporal baselines from simultaneous acquisitions at both frequencies and in particular we discuss the complementary aspects of the two frequencies in terms of sensitivity to line-of-sight displacements and temporal decorrelation in typical measurement scenarios.

1 Introduction

Recently, we have demonstrated car-borne and UAV-borne repeat-pass interferometry-based mobile mapping of surface displacements with an in-house developed compact *L-band* FMCW SAR system [1, 2] which we have deployed 1) on a car and 2) on VTOL UAVs (Scout B1-100 and Scout B-330) by Aeroscout GmbH. In addition, a first successful demonstration of UAV-borne repeat-pass SAR tomography using the very same L-band SAR system has been presented at EUSAR 2021 [3].

We have been further consolidating our experience with repeat-pass SAR interferometry data acquisition, SAR imaging, and interferometric processing from such agile platforms by conducting and analysing several car-borne and UAV-borne repeat-pass interferometry campaigns. Meanwhile we have deployed a dual-frequency car-borne measurement configuration (see **Fig. 1)** that now permits acquiring simultaneously at L-band and at Ku-band using both the Gamma L-band SAR system [1, 2] and a GPRI Ku-band radar [4, 5] with Horn antennas suitable for SAR data acquisition.

The motivation behind this dual-frequency setup is twofold: 1) in steep slopes, which are typical displacement/geohazard monitoring targets for such (quasi-) terrestrial DInSAR systems, the surface is often a mix of bare rock, slightly vegetated patches, and larger vegetation such as bushes and trees. Therefore, frequency diversity is an advantage in terms of temporal decorrelation as illustrated by the decorrelation model by Zebker and Villasenor [6] (see **Fig. 3**). 2) various geomorphological processes may play a role at the same site; potentially, with different orders of magnitudes of surface displacements.

Figure 1: The dual-frequency car-borne SAR setup with (1) the Gamma L-band SAR [1, 2] system with the two (Tx & Rx) white polarimetric patch antennas and (2) the Ku-band GPRI [4, 5] in SAR mode with Horn antennas. The two radar systems can be operated simultaneously. A Honeywell HGuide n580 INS/GNSS system with a local GNSS reference station are used for positioning.

The dual-frequency DInSAR setup can help to better capture the full range of displacements. Stationary terrestrial radar interferometers are well established [7, 8, 9, 10], yet, a car-borne SAR platform can provide a much higher spatial resolution in azimuth. In this paper, we present first results from repeat-pass interferometric acquisitions obtained simultaneously at both frequencies and we discuss the complementary aspects of the two frequencies in terms of sensitivity to line-of-sight displacements and temporal decorrelation in a typical measurement scenario.

ISBN 978-3-8007-5823-4 / ISSN 2197-4403

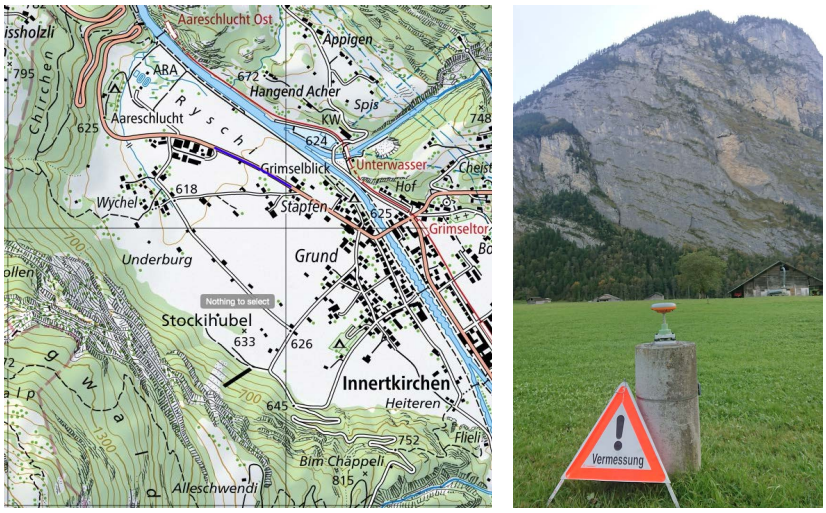

(a) (b)

Figure 2: (a) Map view of the test site. The rock wall in the south-west of the map was repeatedly imaged while driving the dual-frequency car-borne SAR system on a road (blue line). (b) Photo of the rock wall with local GNSS reference station in the foreground. Map data source: © swisstopo.

2 Methods and Data

Tables 1 & 2 provide an overview of the system specifications of the two SAR systems. The L-band radar allows full-pol data acquisitions, single-pass cross-track, along-track interferometric acquisitions and combination of these modes with up to 4 simultaneous receive channels. The Ku-band FMCW SAR system (see Table 2) is based on the Gamma Portable Radar Interferometer (GPRI), a stationary rotational real-aperture radar interferometer [4, 5, 11]. **Fig 2** a) shows a map view of the test site. The rock wall in the south-west of the map was repeatedly imaged while driving the dual-frequency carborne SAR system on the road indicated with a blue line and b) shows a photo of the rock wall with the local GNSS reference station in the foreground.

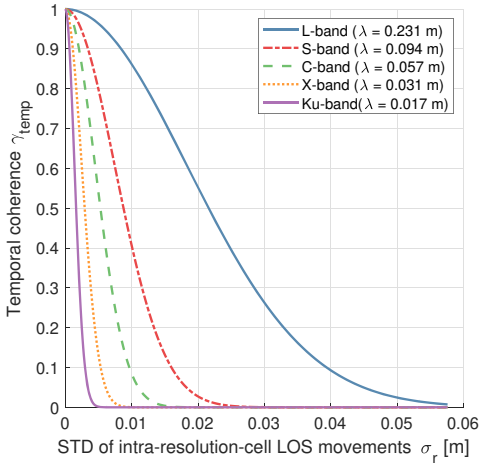

Figure 3: Temporal decorrelation modelled as a function of the standard deviation of the intra-resolution-cell motion in line-of-sight direction $\gamma_{temp}(t) = \exp\left(-\frac{1}{2}\left(\frac{4\pi}{\lambda}\right)^2 {\sigma_r}^2(t)\right)$ after Zebker and Villasenor [6].

Frequency within	1.2 - 1.4 GHz
used center freq.	1.325 GHz
wavelength at center freq.	22.6 cm
Chirp bandwidth	50 - 200 MHz
range res. (@100 MHz BW)	1.5 m
Azim. res. (@ full SA)	$\leq$ 0.5 m
Azim. res. (@ SA=250m, R=5km)	2.3 m
Type	FMCW
Chirp lengths	250 μs - 8 ms.
Transmit power	max. 10W (used: 5W)
Transmit channels	2 (alternating)
Receive channels	4 (simultaneous)
Elev. beamwidth (3dB)	40.0 deg
Azim. beamwidth (3dB)	40.0 deg
Elev. pointing angle	variable (config. dep.)
Radar hardware assembly	Pelicase 1450
Dimensions (l/w/h)	406/330/174 mm
Weight	7.65 kg

Table 1: Gamma L-band SAR specifications

The car-borne SAR imagery is focused with a time-domain back-projection (TDBP) approach [12, 13, 14, 15] parallelized for NVIDIA GPUs [16].

Frequency within	17.1 - 17.3 GHz
used center freq.	17.2 GHz
wavelength at center freq.	1.74 cm
Chirp bandwidth	50 - 200 MHz
range res. (@200 MHz BW)	0.75 m
Type	FMCW
Chirp lengths	250 μs - 8 ms.
ADC sampling rate	6.25 MHz
Elev. beamwidth (3dB)	25.0 deg
Azim. beamwidth (3dB)	12.5 deg

Table 2: GPRI-based Ku-band SAR specifications

ISBN 978-3-8007-5823-4 / ISSN 2197-4403

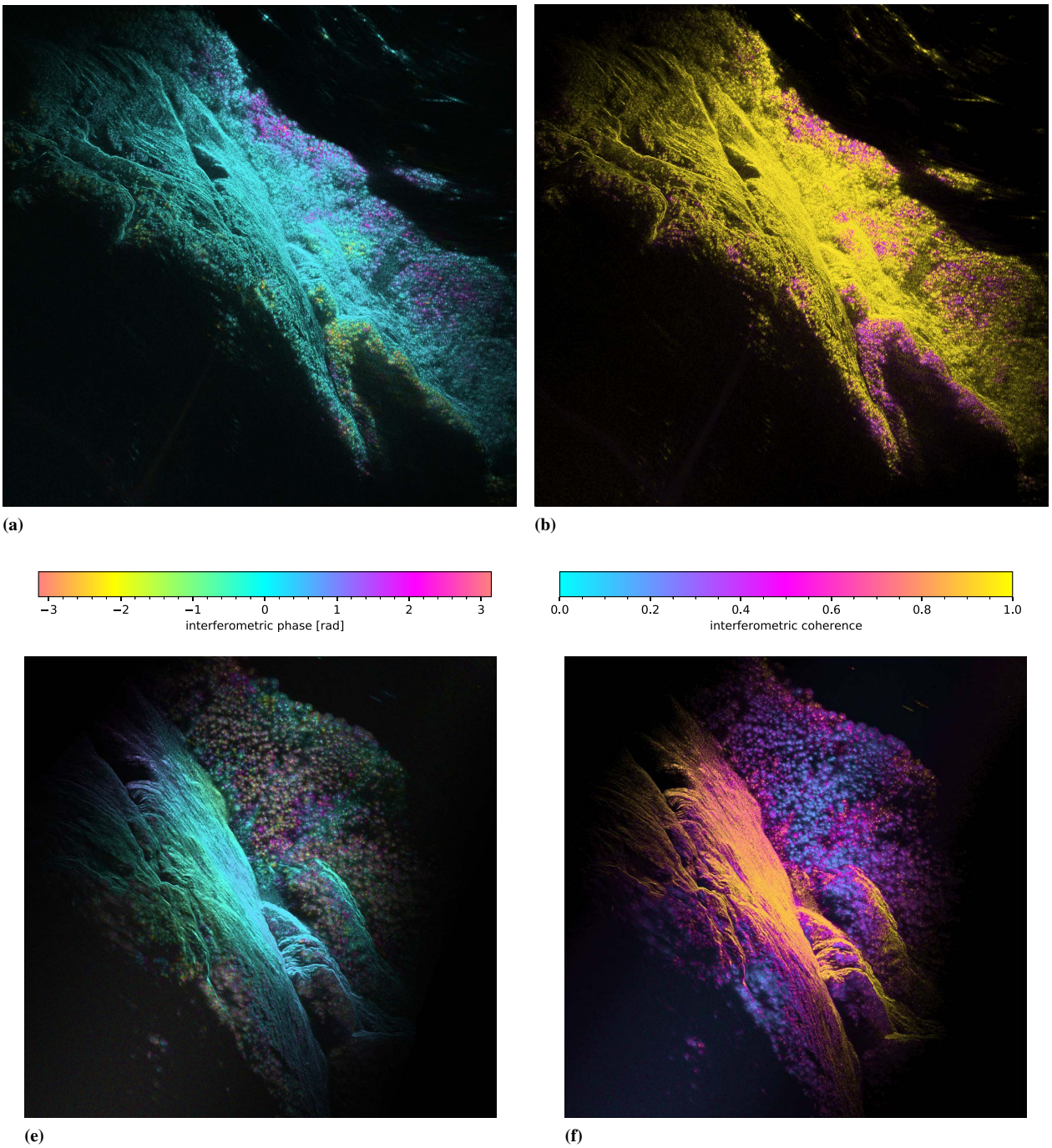

Figure 4: Interferometric phase (a) and coherence (b) obtained from repeated car-borne L-band SAR acquisitions. (e) and (f) show the interferometric phase and coherence for the Ku-band SAR data, obtained simultaneously. The repeat-pass time interval is very short (approx. 4 min). Therefore, no surface displacements were measured during this test. However, the short interval is suitable to check for short-term temporal decorrelation and other phase disturbances, which was the main goal of this first test. The repeat measurements were taken on 2022-02-15 at 13:53 and at 13:57. Interferograms and coherence maps are blended with the backscatter intensity map for visualization purposes. The SAR imagery is processed onto a high-resolution digital elevation model (swissALTI3D, ©swisstopo) and the data is displayed in map coordinates. Note, that the imaged area (and the image patch) is smaller at Ku-band as a result of the narrower azimuth antenna beam width.

3 Results and Discussion

Fig. 4 shows the interferometric phase (a) and the interferometric coherence (b) obtained from repeated car-borne L-band SAR observation of a rock wall and the surrounding area. **Fig. 4** (e) & (f) show the interferometric phase and coherence for the corresponding Ku-band SAR data, which were acquired simultaneously with the L-band SAR imagery. The measurements were taken on 2022-02-15 at 13:53 and at 13:57. A short repeat-pass

ISBN 978-3-8007-5823-4 / ISSN 2197-4403

interval of approx. 4 min was chosen. This means, that no displacements were measured during this test, but the short interval is suitable to check for short-term temporal decorrelation and other phase disturbances. Indeed, and as expected, the L-band and Ku-band data show distinct differences.

At L-band the coherence is very high except in some parts of the forested area, whereas even a large part of the forested area below the rock wall shows a very high coherence (above 0.9 and better). In highly-coherent areas the phase of the L-band interferogram is consistent and remains very stable around zero.

As expected, the coherence is much lower overall at Ku-band. The bare rock wall still shows reasonable coherence whereas vegetated and forested areas are almost completely decorrelated. Clearly, this is in line with the decorrelation model of Zebker and Villasenor [6]: as can be seen in **Fig. 3**, at Ku-band (17.2 GHz), the interferometric signal is entirely decorrelated already for a standard deviation of the intra-resolution-cell motion in LOS direction as small as 5 mm. The interferometric phase at Ku-band shown in **Fig. 4** (e) is spatially smooth within the bare rock area but shows clear phase trends. Due to the short wavelength, error sources such as residual unknown topography (a serious problem in such steep terrain!) in combination with the much stronger spatial baseline criterion at Ku-band and the agile SAR platform, residual unknown motion, and tropospheric variations all become more relevant at this frequency rendering the repeat-pass acquisition at Ku-band more challenging. Nevertheless, the interferometric phase obtained across the rock wall at Ku-band is spatially smooth so that a substantial portion of the unwanted phase variation could be removed by detrending.

We conclude that car-borne repeat-pass DInSAR at Ku-band is feasible with some limitations, currently. This opens the door to benefit from the high sensitivity to line-of-sight displacements at Ku-band in combination with a high spatial resolution available through aperture synthesis with a car-borne InSAR system. We continue the repeat-pass interferometric measurements at this location and we are currently investigating different strategies to further mitigate undesired phase variations found in the car-borne Ku-band InSAR data.

References

[1] O. Frey, C. L. Werner, and R. Coscione, "Car-borne and UAV-borne mobile mapping of surface displacements with a compact repeat-pass interferometric SAR system at L-band," in *Proc. IEEE Int. Geosci. Remote Sens. Symp.*, 2019, pp. 274–277.

[2] O. Frey, C. L. Werner, A. Manconi, and R. Coscione, "Measurement of surface displacements with a UAV-borne/car-borne L-band DInSAR system: system performance and use cases," in *Proc. IEEE Int. Geosci. Remote Sens. Symp.* IEEE, 2021, pp. 628–631.

[3] O. Frey and C. L. Werner, "UAV-borne repeat-pass SAR interferometry and SAR tomography with a compact L-band SAR system," in *Proc. Europ. Conf. Synthetic Aperture Radar, EUSAR*. VDE, March 2021, pp. 181–184.

[4] C. L. Werner, A. Wiesmann, T. Strozzi, A. Kos, R. Caduff, and U. Wegmuller, "The GPRI multi-mode differential interferometric radar for ground-based observations," in *Proc. EUSAR 2012*, Apr. 2012, pp. 304–307.

[5] T. Strozzi, C. L. Werner, A. Wiesmann, and U. Wegmuller, "Topography mapping with a portable real-aperture radar interferometer," *IEEE Geosci. Remote Sens. Lett.*, vol. 9, no. 2, pp. 277–281, Mar. 2012.

[6] H. Zebker and J. Villasenor, "Decorrelation in interferometric radar echoes," *IEEE Trans. Geosci. Remote Sens.*, vol. 30, no. 5, pp. 950–959, Sept. 1992.

[7] G. Luzi, M. Pieraccini, D. Mecatti, L. Noferini, G. Guidi, F. Moia, and C. Atzeni, "Ground-based radar interferometry for landslides monitoring: atmospheric and instrumental decorrelation sources on experimental data," *IEEE Trans. Geosci. Remote Sens.*, vol. 42, no. 11, pp. 2454–2466, Nov. 2004.

[8] A. Aguasca, A. Broquetas, J. J. Mallorqui, and X. Fabregas, "A solid state L to X-band flexible ground-based SAR system for continuous monitoring applications," in *Proc. IEEE Int. Geosci. Remote Sens. Symp.*, vol. 2, Sept. 2004, pp. 757–760.

[9] R. Caduff, F. Schlunegger, A. Kos, and A. Wiesmann, "A review of terrestrial radar interferometry for measuring surface change in the geosciences," *Earth Surface Processes and Landforms*, vol. 40, no. 2, pp. 208–228, 2015.

[10] O. Monserrat, M. Crosetto, and G. Luzi, "A review of ground-based SAR interferometry for deformation measurement," *ISPRS Journal of Photogrammetry and Remote Sensing*, vol. 93, pp. 40–48, 2014.

[11] R. Caduff, A. Kos, F. Schlunegger, B. W. McArdell, and A. Wiesmann, "Terrestrial radar interferometric measurement of hillslope deformation and atmospheric disturbances in the Illgraben debris-flow catchment, Switzerland," *IEEE Geoscience and Remote Sensing Letters*, vol. 11, no. 2, pp. 434–438, Feb. 2014.

[12] O. Frey, C. Magnard, M. Rüegg, and E. Meier, "Focusing of airborne synthetic aperture radar data from highly nonlinear flight tracks," *IEEE Trans. Geosci. Remote Sens.*, vol. 47, no. 6, pp. 1844–1858, June 2009.

[13] A. Ribalta, "Time-domain reconstruction algorithms for FMCW-SAR," *IEEE Geosci. Remote Sens. Lett.*, vol. 8, no. 3, pp. 396–400, May 2011.

[14] C. Stringham and D. G. Long, "GPU processing for UAS-based LFM-CW stripmap SAR," *Photogrammetric Engineering & Remote Sensing*, vol. 80, no. 12, pp. 1107–1115, 2014.

[15] O. Frey, C. L. Werner, U. Wegmuller, A. Wiesmann, D. Henke, and C. Magnard, "A car-borne SAR and InSAR experiment," in *Proc. IEEE Int. Geosci. Remote Sens. Symp.*, 2013, pp. 93–96.

[16] O. Frey, C. L. Werner, and U. Wegmuller, "GPU-based parallelized time-domain back-projection processing for agile SAR platforms," in *Proc. IEEE Int. Geosci. Remote Sens. Symp.*, July 2014, pp. 1132–1135.

ISBN 978-3-8007-5823-4 / ISSN 2197-4403